Particle Size Information from Dispersed Phase Photoemission Intensity Ratios

S. Mark Davis

Exxon Research and Development Laboratories, P.O. Box 2226, Baton Rouge, Louisiana 70821

A simple method for obtaining particle size information from photoemission results is formulated by considering the intensity ratio for two dispersed phase core levels with different kinetic energy. This analysis predicts a high sensitivity for detecting particle size differences for sizes in the range of about $0.4\lambda \le d \le 2\lambda$, where λ is the photoelectron attenuation length, i.e., particle sizes in the range of about 10–50 Å. A major advantage of this approach over earlier methods involving the dispersed phase to support phase intensity ratio is a reduced dependence on surface roughness and physical properties of the catalyst. Example applications suggest that many opportunities exist for applying this analysis in studies of multicomponent practical catalysts. © 1989 Academic Press, Inc.

INTRODUCTION

X-ray photoelectron spectroscopy (XPS) has evolved as one of the most valuable surface science tools for studies of the chemical state and surface composition of heterogeneous catalysts. In contrast to chemisorption, microscopy, or X-ray diffraction methods, photoemission can be conveniently applied to differentiate highly dispersed metal oxide and sulfide compounds as well as reduced metals and, in favorable cases, the nature of the metal–support electronic interaction. Despite these successes, the full potential that photoemission results offer for investigation of the *size* of dispersed phase particles has generally not been recognized. In 1979, Fung (1) developed a flat-surface model for estimating particle size from the (dispersed phase/support phase) XPS intensity ratio that was an extension of the method previously advanced by Angevine et al. (2) and Fadley et al. (3). At about the same time, Kerkhof and Moulijn (4) proposed a more realistic model for high-area materials which represented the catalyst as a series of slabs supporting cubic dispersed phase particles. The utility of these methods was demonstrated in a variety of applications

including studies of platinum sintering on silica (1) and the monolayer-like dispersion of Na/Al_2O_3 (2), F/Al_2O_3 (3), and WO_3/Al_2O_3 (1).

In this report we propose a complementary method for particle size estimation for photoemission results that is based on the intensity ratio for two dispersed phase core levels with different kinetic energy. A major advantage of this approach over methods utilizing the (metal/support) intensity ratio is a greatly reduced dependence on surface roughness and physical properties of the catalyst such as support surface area and dispersed phase loading and distribution.

BASIC CONCEPTS

We begin by considering the primary photoemission intensity for a species i in the near-surface region of a solid that can be expressed by (3)

$$\frac{dI_i}{dV} = F_0 k_i H_i G T_i \exp\left(-\frac{z}{\lambda_i}\right). \qquad (1)$$

Here F_0 is the X-ray flux; k_i is a spatial distribution function; H_i is a spectroscopic constant which includes the atomic density, the photoionization cross section, and its angular distribution; G is a physical con-
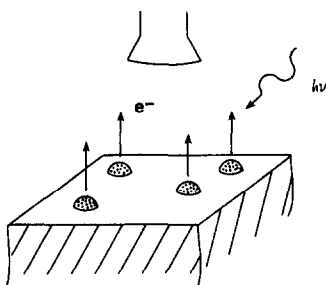
432

FIG. 1. Schematic diagram depicting normal emission from hemispherical dispersed phase particles on a thick, planar support.

stant that depends on the shape and roughness of the surface; T_i is an instrumental factor that reflects the basic detection efficiency; z is the distance into the solid surface; λ_i is the attenuation length of the primary photoelectrons; and dV is a differential volume element of the solid. For conditions under which the researcher investigates emission normal to the macroscopic surface with a typical pass energy analyzer employing preretardation, Eq. (1) is well approximated by

$$\frac{dI_i}{dV} = \rho_i \sigma_i T_i \exp\left(-\frac{z}{\lambda_i}\right), \qquad (2)$$

where ρ_i is the atomic density and σ_i is the photoionization cross section.

An idealized model catalyst is represented in Fig. 1 in which a dispersed phase is deposited on a flat, infinitely thick support surface. In this circumstance, Eq. (2) can be easily integrated for any regular particle shape to yield an equation of the form

$$I_i(d) = \rho_i \sigma_i T_i \lambda_i A_0 F(L, s, d)\beta(d, \lambda_i), \quad (3)$$

where A_0 is the analyzed area, $F(L, s, d)$ is the fraction of the support surface area covered by the dispersed phase, and $\beta(d, \lambda_i)$ is an attenuation factor which is characteristic of the particle shape and photoelectron attenuation length. As discussed previously (1), $F(L, s, d)$ is a function of the dispersed phase loading, L, support surface area, s, and particle size, d, along with the dispersed phase bulk density, D. The functional forms of $F(L, s, d)$ and $\beta(d, \lambda)$ are summarized in Table 1 for a variety of regular particle shapes (1). It follows that the intensity ratio for the two dispersed phase core levels is simply given by

$$\frac{I_1(d)}{I_2(d)} = \frac{\sigma_1 T_1 \lambda_1 \beta(d, \lambda_1)}{\sigma_2 T_2 \lambda_2 \beta(d, \lambda_2)}, \qquad (4)$$

TABLE 1

Particle Shapes, Fractional Surface Coverages, and Attenuation Factors for XPS Determination of Average Particle Size

Particle shape	Dimensions	Fractional coverage $F(L, s, d)$	Attenuation factors $\beta(d, \lambda)$
Cube	d = edge length	L/Dsd	$1 - \exp(-d/\lambda)$
Raft or disk	d = diameter h = height	L/Dsh	$1 - \exp(-h/\lambda)$
Prism	c = length a = base width h = height	$2L/Dsh$	$1 - (\lambda/h)[1 - \exp(-h/\lambda)]$
Pyramid	d = base edge length h = height	$3L/Dsh$	$1 - (2\lambda^2/h^2)[\exp(-h/\lambda) + h/\lambda - 1]$
Cone	d = base diamter h = height	$3L/Dsh$	$1 - (2\lambda^2/h^2)[\exp(-h/\lambda) + h/\lambda - 1]$
Sphere	d = diameter	$3L/2Dsd$	$1 - (2\lambda^2/d^2)[1 - \exp(-d/\lambda)] + (2\lambda/d) \exp(-d/\lambda)$
Hemisphere	d = diameter	$3L/Dsd$	$1 - (8\lambda^2/d^2)[1 - \exp(-d/2\lambda)] + (4\lambda/d) \exp(-d/2\lambda)$

where the subscripts correspond to the two dispersed phase XPS peaks. In the simplest case of cubic crystallites, $\beta(d, \lambda) = 1 - \exp(-d/\lambda)$, and average particle size is obtained by iteration of

$$d = -\lambda_1 \ln \left[1 - \frac{\sigma_2 T_2 \lambda_2 I_1}{\sigma_1 T_1 \lambda_1 I_2} \right.$$
$$\left. \times \left(1 - \exp\left(-\frac{d}{\lambda_2}\right)\right)\right]. \quad (5)$$

Similar relations may be easily derived for other particle shapes using the $\beta(d, \lambda)$ functions summarized in Table 1.

Comparison of Eqs. (3) and (4) reveals an important advantage for this method compared to that based on the (metal/support) intensity ratio. Specifically, the intensity ratio for two dispersed phase XPS peaks eliminates the dependence on physical properties of the catalyst such as support surface area, dispersed phase loading and density, and the dispersed phase spatial distribution throughout the pore structure of the support. The latter consideration is especially appealing as it is typically very difficult to ascertain the dispersed phase distribution on an atomic scale.

The sensitivity of this approach for detecting particle size changes is illustrated in Fig. 2 where the ratio $\beta(d, \lambda_2)/\beta(d, \lambda_1)$ is plotted as a function of particle size in dimensionless units of λ_2. In the top frame, the ratio of attenuation factors for small particles with cubic morphology is considered for different ratios of the electron attenuation lengths with $\lambda_1/\lambda_2 = 0.3$–$0.75$. As λ_1/λ_2 decreases, the ratio of attenuation factors becomes a strong function of particle size for average sizes in the range of about 0.4 to $2\lambda_2$. With $\lambda_2 \sim 25$ Å, the range of detectable particle sizes becomes about 10 to 50 Å. Since for energies above about 50 eV, λ is a slowly varying function of electron energy with an approximate dependence $\lambda \sim E^{1/2}$ (5), it is clear that for small differences in particle size to be distinguishable, the photoemission peaks chosen for analysis must differ as much as possible in
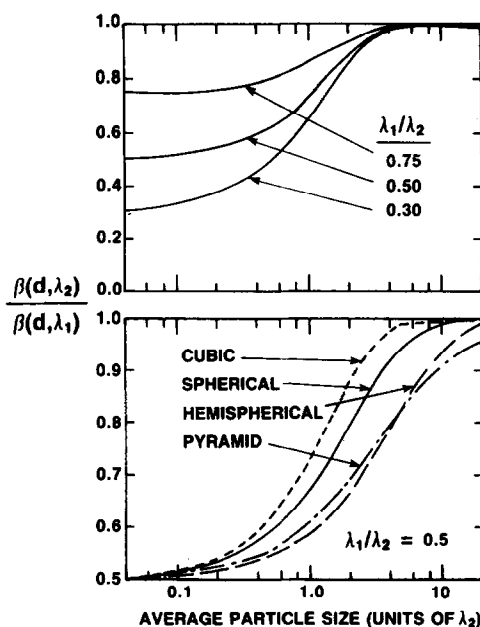

FIG. 2. The ratio of attenuation factors for two dispersed phase XPS peaks with different kinetic energy is plotted as a function of the average dispersed phase particle size expressed in units of λ_2 where $\lambda_2 > \lambda_1$. In the top frame cubic particles are considered and λ_1/λ_2 is varied from 0.3 to 0.75. In the lower frame, different particle shapes are considered with $\lambda_1/\lambda_2 = 0.5$ fixed.

photoelectron energy. This constraint appears to be the major limitation associated with this approach. In practice, with typical magnesium and aluminum X-ray sources, this constraint eliminates a variety of elements including Li, Al, Si, P, Br, Sr, Y, Zr, and the $5d$-transition metals. Fortunately, however, by combination of low-energy XPS or X-ray-excited Auger peaks with high-kinetic-energy XPS core levels, most catalytically active metals and compounds can be studied.

Another constraint which becomes important for catalysts with low loadings and/ or large particle sizes is that the XPS peaks chosen for analysis must have sufficiently high cross section and sharp peak shape so that the peak areas can be measured. Experience indicates that loadings of 1–2 wt% are frequently accessible by this approach, although higher loadings may be required in

TABLE 2

Elements and XPS Peaks Suitable for Analysis
Using Dispersed Phase Intensity Ratios

Elements	Low-kinetic-energy peak	High-kinetic-energy peak	Approximate[a] (λ_1/λ_2)
C, N, O	KLL	1s	0.43–0.71
F, Na, Mg	1s	2s	0.70–0.33
S, Cl, K, Ca	LMM	2p	0.22–0.52
Ti, V, Cr	$L_3M_{23}V$	2p or 3p	0.61–0.55
Mn, Fe, Co, Ni, Cu, Zn, Ga, Ge, As	2p	3p	0.75–0.30
Nb, Mo	$M_{45}N_{23}V$	3d	0.31–0.34
Ru, Rh, Pd, Ag	$M_{45}VV$	3d	0.45–0.53
Cd, In, Sn	$M_{45}N_{45}N_{45}$	3d or 4d	0.57–0.52
Sb, Te, I, Cs, Ba, La, Ce	3d	4d	0.78–0.65
Pb, Bi, Th, U	NOV or 4d	4f or 5d	0.27–0.85

[a] With Al$K\alpha$ X-rays.

some applications. Table 2 summarizes photoemission peaks and approximate attenuation length ratios for catalytically relevant elements.

In the lower frame of Fig. 2 the ratio of attenuation factors $\beta(d, \lambda_2)/\beta(d, \lambda_1)$ is plotted as a function of particle size for several different particle shapes with λ_1/λ_2 held constant. While there is a dependence on particle shape, much of the variation indicated in Fig. 2 arises from our definition of the particle size as an edge length or diameter. For the region of Fig. 2 where $d = 1–2\lambda_2$, with the absolute number of atoms contained in the crystallites of different shape constrained to be constant, it can be easily shown that $(\beta_2/\beta_1)_{cube} \approx 1.15(\beta_2/\beta_1)_{sphere} \approx 1.6(\beta_2/\beta_1)_{hemisphere}$. Thus for a fixed volume, decreasing the particle thickness has a significant influence on (β_2/β_1), especially for small particle sizes. In practice, apparent particle size changes must usually be referred to a particular particle shape which is assumed to be constant. This assumption can be justified only by the application of complementary characterization techniques that are sensitive to the particle morphology.

EFFECT OF CONTAMINANT OVERLAYERS

A complicating feature of particle size estimation from photoemission data is that the presence of contaminant overlayers on the surfaces of interest can have a significant impact on the particle size prediction. In this case, Eqs. (1)–(3) are modified by the factor $\exp(-t/\lambda_c)$ which reflects the attenuation of primary intensity by a contaminant overlayer with thickness t and an attenuation length λ_c which is characteristic for this species. To estimate the magnitude of this effect, we consider the influence of a contaminant overlayer with thickness $t = 0.1–0.3\lambda_2$ on the calculated $I_1(d)/I_2(d)$ ratios for cubic crystallites. Similar reasoning should apply to alternate particle shapes. It should be recalled that contaminant overlayers can also adversely influence particle size predictions on the basis of the dispersed phase/support phase XPS intensity ratio (I).

In the presence of a contaminant overlayer the photoemission peak with lower kinetic energy tends to be preferentially attenuated. Figure 3 illustrates the influence of this preferential attenuation on the $\beta(d,$
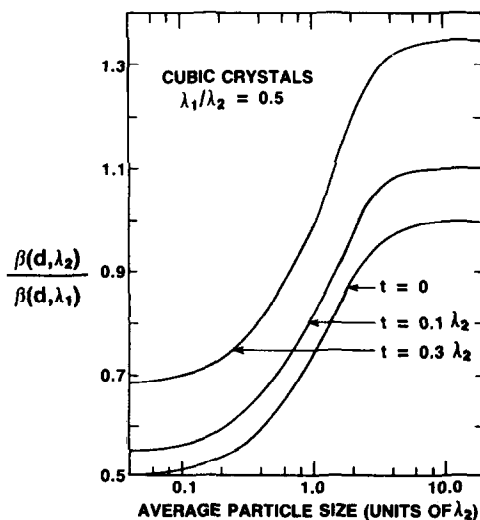

FIG. 3. The ratio of attenuation factors for two dispersed phase photoelectron peaks with $\lambda_1/\lambda_2 = 0.5$ has been plotted for cubic particles as a function of average particle size expressed in units of λ_2. The presence of a contaminant overlayer with thickness t causes the ratio of attenuation factors to deviate significantly from that predicted for a clean surface.

$\lambda_2)/\beta(d, \lambda_1)$ ratio for cubic crystallites with $\lambda_1 = \lambda_2/2$ and the approximation that $\lambda_1 = \lambda_c$. The presence of a contaminant overlayer increases the measured $\beta(d, \lambda_2)/\beta(d, \lambda_1)$ ratio which will lead to the prediction of a larger particle size than is actually present. This effect is particularly pronounced with smaller particle sizes and large overlayer thicknesses. It is clear from Fig. 3 that for Eq. (4) to have predictive value, considerable caution must be exercised to ensure surface cleanliness. Carbon contamination can best be eliminated by combining clean pretreatment and UHV facilities with reasonably short data acquisition times. It is also apparent that analysis of dispersed phase intensity ratios will generally provide an *upper limit* to the true average particle size. The effect of overlayers may complicate applications with multicomponent systems where the primary dispersed phase is "decorated" by a second species or becomes encapsulated by the support. Metal exchanged zeolites, for example, can be viewed as a limiting case of the latter situation. Systems of this type are not amenable to meaningful analysis by this approach.

EFFECT OF SURFACE ROUGHNESS

Up to now we have assumed an idealized support surface that is flat and continuous. While this situation can be largely realized in experimental studies of model catalysts, practical catalysts are rough on an atomic scale regardless of the method of sample preparation. The problem of roughness and its effect on the angular distribution of XPS intensities has been considered in detail by Fadley *et al.* (*3*) for uniform overlayers on a one-dimensional sinusoidal surface. In this section a similar analysis is developed for "broken overlayers" represented by spherical and cubic particles dispersed on one-dimensional triangular support surfaces as exemplified in Fig. 4. Whereas the (metal/support) intensity ratio shows a marked sensitivity to surface roughness (*3, 6*) we demonstrate that the intensity ratio
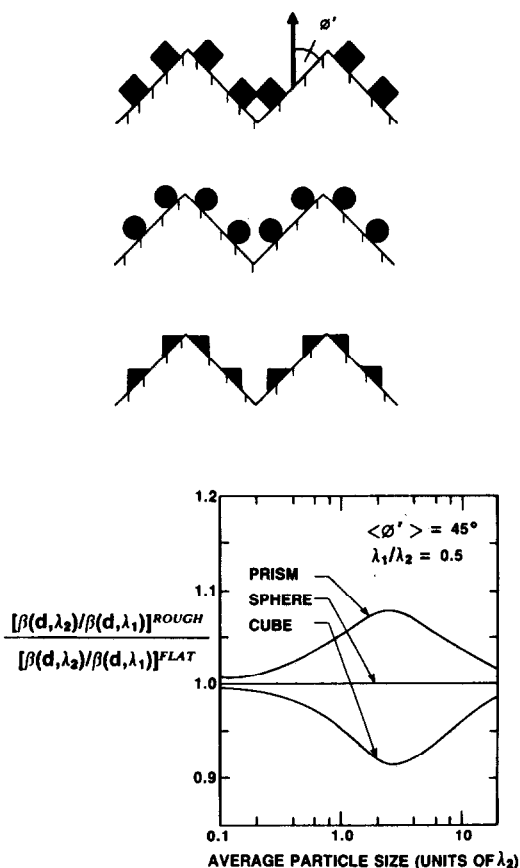

FIG. 4. Idealized models for one-dimensional rough surfaces showing triangular support surfaces partially covered by cubic, prismatic, or spherical dispersed phase particles. Roughness causes the average electron escape angle to deviate from 90°. The ratio of attenuation factors for two dispersed XPS peaks has also been calculated for the triangular surfaces and compared as a function of particle size with the corresponding ratio for a flat surface. Different curves reflect variable particle shapes with $\langle \phi' \rangle = 45°$ and $\lambda_1/\lambda_2 = 0.5$ constrained constant.

for two dispersed phase core levels is only slightly altered by surface roughness.

As discussed previously (*3*), the major effects of surface roughness are to shadow certain regions of the surface and to alter the electron escape angle from the flat surface value. At any point along the rough surface, the true escape angle ϕ' (cf. Fig. 4) is defined as the angle between the escape direction and the microscopic surface tan-

gent. The average angle of emission $\langle \phi' \rangle$ in general will not equal the macroscopic take-off angle ϕ which we have assumed for simplicity to equal 90°.

In Fig. 4, the ratio $\beta(d, \lambda_2)/\beta(d, \lambda_1)$ for surfaces with triangular roughness and $\langle \phi' \rangle$ = 45° is compared as a function of particle size with the corresponding ratio for an ideal flat surface. Three particle shapes are considered, namely, right prisms, spheres, and cubes, with $\lambda_1/\lambda_2 = 0.5$. The attenuation factor for spherical particles shows no dependence on $\langle \phi' \rangle$, and therefore $\beta(d, \lambda_2)/\beta(d, \lambda_1)$ is not changed for a rough surface. However, for $\langle \phi' \rangle < 90°$, the attenuation factor for cubic particles decreases. Specifically, for a cubic particle on a one-dimensional triangular support, Eq. (2) may be integrated for any angle $\langle \phi' \rangle$ to yield (Appendix A),

$$I(d, \phi')$$

$$= \rho\sigma T\lambda d^2 2 \cos \phi' \left[1 - \frac{1}{2}\left(1 - \tan \phi' \right.\right.$$

$$\left. + \frac{2\lambda}{(\sin \phi' + \cot \phi' \cos \phi')d} \right) \left(1 \right.$$

$$\left.\left. - \exp\left(-\frac{(\sin \phi' + \cot \phi' \cos \phi')d}{\lambda} \right) \right) \right].$$

$$(6)$$

In the special case where $\langle \phi' \rangle$ = 45° and $\sin^2 \phi' \geq F(L, s, d)$ so that no shadowing of the dispersed phase particles occurs,

$$\beta'(d, \lambda) = 1 - \frac{\lambda}{\sqrt{2}d}\left(1 - \exp\left(-\frac{\sqrt{2}d}{\lambda} \right) \right).$$

$$(7)$$

Comparison of Figs. 2 and 4 indicates that roughness causes the cubic particles to appear more like spheres or pyramids. By contrast, the attenuation factor for prismatic particles increases for $\langle \phi' \rangle < 90°$, causing $\beta(d, \lambda_2)/\beta(d, \lambda)$ to increase slightly. As such, the prismatic particles appear more like cubes. In any event, the effect of roughness is relatively small in all cases. The deviation from flat surface behavior becomes even smaller for $\langle \phi' \rangle \neq 45°$.

The basic conclusions developed here for surfaces with triangular roughness should be broadly applicable to rough surfaces with alternate shapes such as semicircular or sinusoidal roughness and surfaces characterized by two-dimensional roughness. Significant enhancement of the dispersed phase intensity relative to the support is expected in all cases where $\langle \phi' \rangle < \phi$ (6), whereas the intensity ratio for two dispersed phase core levels shows little dependence on $\langle \phi' \rangle$.

HIGH-AREA SUPPORTS

Throughout this analysis it was assumed that the support particles were large in size with a thickness b such that $b \gg \lambda$. This assumption was adopted so that there would exist no contribution to the dispersed phase intensity for species located in microporous regions below the surface. In practice, however, catalyst supports frequently exhibit very high surface areas so that the assumption $b \gg \lambda$ is not valid. In this section, we explore the consequences of a high support surface area ($b \simeq \lambda_s$) and its effect on particle size predictions using two models illustrated in Fig. 5. The first model follows that proposed by Kerkhof (4) wherein the catalyst is constructed of infinite slabs with thickness b and dispersed phase particles distributed on both upper and lower surfaces. In the second case, the support is based on a loosely packed array of diamond-shaped particles with $\langle \phi' \rangle$ = 45°. In both cases, we assume a random registry between layers of support material and a dispersed phase loading small enough that self-attenuation of the dispersed phase intensity by dispersed phase particles in alternate layers may be neglected. With these constraints, the dispersed and support phase intensities can be conveniently evaluated using a layer-by-layer analysis that is developed in Appendix B. For the slab model the dispersed phase intensity ratio for the multilayer (ML) catalyst relative to the single-layer (SL) system represented by Eq. (4) becomes
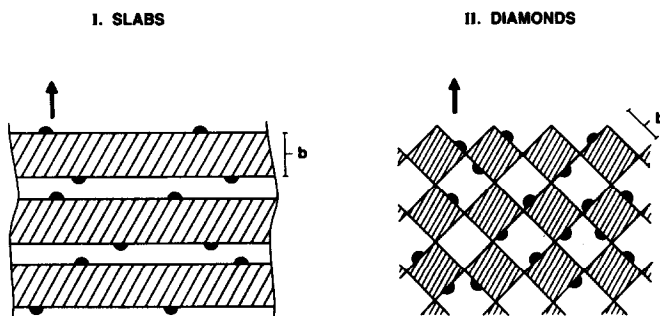
FIG. 5. Idealized slab and diamond models for XPS characterization of dispersed phase particle size in high area heterogeneous catalysts. While the diamond layers are shown to be in registry, this is not a requirement of the model.

$$\frac{(I_1(d)/I_2(d))^{ML}}{(I_1(d)/I_2(d))^{SL}} = \frac{1 + 2/(\exp(b/\lambda_{1s}) - 1)}{1 + 2/(\exp(b/\lambda_{2s}) - 1)}, \qquad (8)$$

where λ_{1s} and λ_{2s} denote attenuation lengths for electrons of energy E_1 and E_2 in the support material, respectively. The corresponding relationship for the diamond model follows from Eq. (7) as

$$\frac{(I_1(d)/I_2(d))^{ML}}{(I_1(d)/I_2(d))^{SL}}$$

$$= \frac{1 + 2/(\sqrt{2}b/\lambda_{1s}(1 - \exp(-\sqrt{2}b/\lambda_{1s})) - 1)}{1 + 2/(\sqrt{2}b/\lambda_{2s}(1 - \exp(-\sqrt{2}b/\lambda_{2s})) - 1)} \qquad (9)$$

In Fig. 6 the intensity ratios represented by Eqs. (8) and (9) are displayed as a function of the support particle size b using the universal curve approximation that $\lambda_s = \lambda_m$. It should be recognized that the dependence shown in Fig. 6 arises because subsurface contributions to the dispersed phase intensity are enhanced for the XPS peak with higher kinetic energy. The deviation from single-layer behavior is substantial for small support particle sizes but becomes negligible for $b \geq 10\lambda$. The deviation from single-layer behavior is enhanced for the diamond model because the average attenuation per layer of support is reduced in this case. Directionally, this effect is similar to that associated with contaminant over-

layers wherein the dispersed phase XPS intensity ratio represents an upper limit to the true particle size.

Practical catalysts may be expected to exhibit behavior intermediate between the slab and the diamond model. In this case, significant deviations from single-layer, infinite-support behavior should occur for $b < \sim 5\lambda_s$. Since λ_s is typically about 20 Å, a practical lower limit to the support particle size for meaningful application of Eq. (4) would appear to be about 100 Å. It is nota-
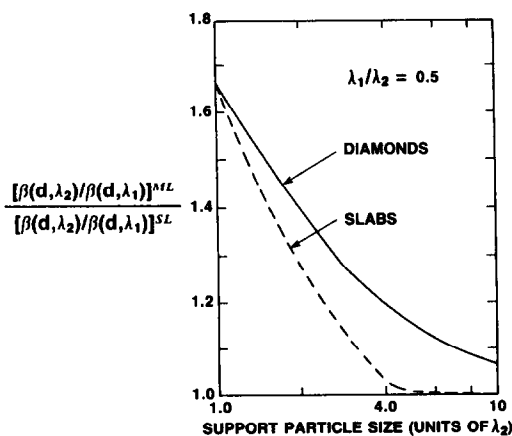

FIG. 6. The ratio of attenuation factors for two XPS peaks with $\lambda_1/\lambda_2 = 0.5$ has been calculated for cubic dispersed phase particles in a multilayer catalyst and compared as a function of the support particle size with the corresponding ratio for a flat, infinite support surface.

ble that this particle size is typical of that for many high-area supports such as SiO_2, γ-Al_2O_3 (160 m²/g, $b \sim 100$ Å), or anatase-TiO_2 (80 m²/g, $b \sim 180$ Å). For spherical or cubic particles, b can be conveniently estimated using $b = 6/sD_s$, where D_s is the support bulk phase density. Alternatively, with slabs, $b = 2/sD_s$.

PARTICLE SIZE AVERAGING

Fung (1) previously emphasized that particle sizes obtained from the (dispersed phase/support phase) XPS intensity ratio are intermediate between a surface and a volume average. A similar interpretation is appropriate for particle sizes estimated from dispersed phase intensity ratios. This behavior arises because subsurface atoms contribute strongly to the observed XPS intensity. However, in the limit of large particle sizes, $\langle d_{xps} \rangle$ tends toward a surface average.

The range of particle sizes where this change in averaging behavior takes place can be clearly understood by considering simple particle size distributions. As exam-

ples, we consider two model distributions of cubic particles, namely, a simple flat distribution, $N(d) = $ constant, and a distribution that varies according to $1/d^2$ over the particle size range from d_{min} to d_{max}. For the flat particle size distribution, the average XPS intensity per particle is given by

$$\langle I_{xps} \rangle = \frac{\rho\sigma T\lambda}{(d_{max} - d_{min})} \left[\frac{d_{max}^3 - d_{min}^3}{3} \right.$$
$$+ \lambda \left[d_{max}^2 \exp\left(-\frac{d_{max}}{\lambda}\right) - d_{min}^2 \right.$$
$$\left. \exp\left(-\frac{d_{min}}{\lambda}\right) \right] + 2\lambda^2 \left[d_{max} \exp\left(-\frac{d_{max}}{\lambda}\right) \right.$$
$$\left. - d_{min} \exp\left(-\frac{d_{min}}{\lambda}\right) \right] + 2\lambda^3 \left[\exp\left(-\frac{d_{max}}{\lambda}\right) \right.$$
$$\left. \left. - \exp\left(-\frac{d_{min}}{\lambda}\right) \right] \right], \quad (10)$$

while for the $1/d^2$ distribution,

$$\langle I_{xps} \rangle = \frac{\rho\sigma T\lambda}{(d_{min}^{-1} - d_{max}^{-1})} \left[(d_{max} - d_{min}) \right.$$
$$\left. + \lambda\left(\exp\left(-\frac{d_{max}}{\lambda}\right) - \exp\left(-\frac{d_{min}}{\lambda}\right) \right) \right]. \quad (11)$$

For both distributions, the average XPS particle size is obtained from successive approximations of

$$\langle d_{xps} \rangle =$$
$$-\lambda \ln(1 - \langle I_{xps} \rangle / \rho\sigma T\lambda \langle d_{xps} \rangle^2). \quad (12)$$

In Fig. 7, the average XPS particle size has been calculated and divided by the number average size and plotted as a function of d_{max} in the case where $d_{max}/d_{min} = 10$. For both distributions the left intercept corresponds to within 1% of the volume average size, whereas the right intercept corresponds very closely with the surface average size. The change in $\langle d_{xps} \rangle$ from a volume to a surface average size clearly takes place in the particle size range where $0.4\lambda < d < 10\lambda$. An entirely similar conclusion results when alternate particle shapes and particle size distributions are considered.

PRACTICAL CONSIDERATIONS

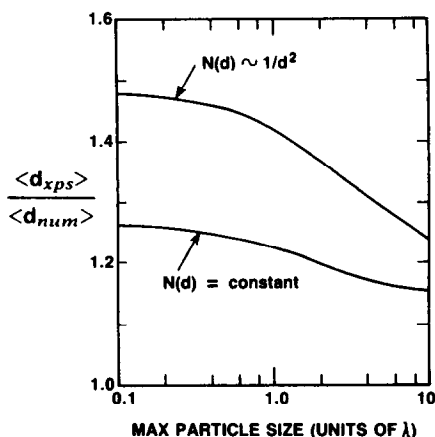The present work combined with earlier reports (1, 4) indicates that a variety of

FIG. 7. The XPS average particle size has been divided by the number average particle size for two model distributions of cubic particles and plotted as a function of the maximum particle size where $d_{max} = 10$ d_{min}. At the left intercept, $\langle d_{xps} \rangle$ corresponds closely with the volume average particle size, whereas at the right intercept, $\langle d_{xps} \rangle$ can be equated with the surface average particle size.

methods exist for obtaining particle size information from photoemission results. A major advantage of the XPS technique is that it can be applied to a variety of highly dispersed compounds that are generally not suitable for analysis by other methods. Major disadvantages of the XPS methods include the requirement of an assumed particle morphology and the sensitivity of the predicted particle size to the presence of contaminant overlayers and/or roughness and catalyst physical properties $(1, 4, 6)$. As such, it is clear that particle sizes predicted from photoemission data are not very exact and are best considered only semiquantitative. Nevertheless, the ability to ascertain particle size differences in an approximate manner is frequently desirable in connection with combined surface science and catalysis studies. As with other approaches for particle size determination, the XPS technique is most valuable when utilized in conjunction with a complementary method such as chemisorption, X-ray line broadening, or electron microscopy.

Quantitative analysis of photoemission data requires accurate knowledge of the primary peak areas and the electron attenuation length λ. While there is evidence that for many materials $\lambda(E)$ is a largely universal function (5), significant differences in λ-values have been reported by different workers $(5, 7–10)$, and there is no consensus as to which values are most appropriate. The formulas proposed by Seah and Dench (5) and Powell et al. (10) frequently produce satisfactory results when applied in particle size evaluations. For simplicity, a nonlinear background which increases according to the integrated photoelectron intensity is commonly adopted to obtain the intensity of the primary peak plus all obvious shake-up satellite features (11). This method normally gives primary intensity estimates not too different from rigorous theory (12). When a consistent background subtraction procedure is applied, reliable, relative values for $\sigma T\lambda$ can be obtained for a given spectrometer from studies of well-

defined bulk compounds, preferably foils or single crystals. It is hoped that future research will provide better guidelines for the utilization of peak intensities and attenuation lengths.

EXAMPLE APPLICATIONS

The approach developed in this report has been utilized to investigate dispersed phase dispersion in a variety of model and practical catalysts. We now consider example applications in studies of F/Al_2O_3 and oxidic and reduced forms of Pd/Al_2O_3. These studies were carried out in a Leybold–Heraeus apparatus designed for combined surface analysis and catalysis studies (13). The materials were investigated as thin pressed wafers (ca. 2 cm^2 × 0.2 mm) mounted on copper or boron nitride sample holders which could be transferred between the reactor and the analysis chamber using magnetic manipulators. Photoemission data were collected using unmonochromatized $AlK\alpha$ (1486.6 eV) or $MgK\alpha$ (1253.6 eV) radiation and hemispherical analyzers which were operated at 50 eV pass energy. All data acquisitions and manipulations were carried out digitally using an HP 1000 computer equipped with the LH-DS5 software package.

F/Al_2O_3

As an example application in studies of highly dispersed species, Table 3 compares $F(2s)/F(1s)$ XPS intensity ratios for F/Al_2O_3 catalysts containing 1.5–7.0 wt% fluorine with the corresponding ratio for the bulk compound α-AlF$_3$. The F/Al_2O_3 materials were prepared by aqueous impregnation of Cyanamid γ-Al$_2$O$_3$ with dilute NH$_4$F to the point of incipient wetness followed by overnight drying in a vacuum oven to 120–140°C. Photoemission studies were carried out using both $AlK\alpha$ and $MgK\alpha$ radiation without further pretreatment. The α-AlF$_3$ (anhydrous, purified MCB) was single phased and stoichiometric as measured by XPS and powder X-ray diffraction. Photoemission and low-energy helium ion scat-

TABLE 3

XPS Intensity Ratios and Particle Size Information
for F/Al$_2$O$_3$

Material	F(2s)/F(1s) · XPS intensity ratio[a]		Dispersed phase thickness[b] (Å)	
	AlKα	MgKα	AlKα	MgKα
1.5% F/Al$_2$O$_3$	0.037	0.030	≤3	≤3
7.0% F/Al$_2$O$_3$	0.041	0.035	15	7
AlF$_3$	0.047	0.045	—	—

[a] ±ca. 10%, kinetic energies for AlKα, F(1s) = 800 eV, F(2s) = 1456 eV; for MgKα, F(1s) = 570 eV, F(2s) = 1220 eV.

[b] Estimated using diamond model with b = 88 Å, λ_{1s}^{Al} = 17.4 Å, λ_{2s}^{Al} = 25.4 Å, λ_{1s}^{Mg} = 14.2 Å, and λ_{2s}^{Mg} = 22.7 Å (14).

tering further revealed that the surface was clean apart from very low levels of carbon, oxygen, and sodium.

It is evident from Table 3 that the F(2s)/F(1s) XPS intensity ratio for 1.5% F/Al$_2$O$_3$ was lowered relative to AlF$_3$ approximately in proportion to the ratio of electron attenuation lengths ($\lambda_{2s}/\lambda_{1s}$ ≈ 0.63 for $h\nu$ = 1253.6 eV; $\lambda_{2s}/\lambda_{1s}$ ≈ 0.69 for $h\nu$ = 1486.6 eV). As such, it appears that fluorine is highly dispersed in this material with an average dispersed phase thickness of about 3 Å or less. By contrast, with 7.0% F/Al$_2$O$_3$ the measure intensity ratio was increased significantly. Applying the diamond model with a raft-like dispersed phase morphology as represented by a combination of Eqs. (3), (7), and (9), the average thickness of the fluorine-containing phase in this catalyst can be estimated to be in the range 7–15 Å (Table 3). Minor differences in the predictions using MgKα and AlKα radiation are within the experimental uncertainty of the intensity ratio measurements. It should be noted that these predictions compare favorably with earlier studies of fluorided aluminas by Kerkhof and Moulijn (4). On the basis of the magnitude of the (F/Al) XPS intensity ratio, these workers proposed that fluorine was present with high, monolayer-like dispersion for loadings up to about 4 wt%. However, at higher loadings, the (F/Al) XPS intensity ratio was reduced presumably due to fluorine incorporation in subsurface sites or nucleation of microscopic aluminum fluoride islands. Our studies also appear to be consistent with this interpretation. Fluorided alumina represents an excellent example of a catalyst application where it would be difficult to obtain fluorine dispersion information using alternate characterization techniques. Moreover, in this example, the F(1s) and F(2s) electron attenuation lengths are not too different.

Pd/Al$_2$O$_3$

As a second example, we consider XPS results for a 3.3% Pd/Al$_2$O$_3$ catalyst that was prepared by incipient wetness impregnation of Al$_2$O$_3$ (66 m^2/g, precalcined 1000°C) with Pd(NH$_3$)$_4$(NO$_3$)$_2$ followed by vacuum drying at 120°C and air calcination at 250–600°C. Photoemission results for as prepared, oxidic forms of the catalyst were collected using both MgKα and AlKα radiation, whereas only AlKα radiation was used following *in situ* reduction for 2 hr at 500°C and atmospheric pressure. Figure 8 shows representative Pd(3d) and Pd(MNN) XPS results for reduced catalysts. Table 4 summarizes XPS intensity ratios for calcined and reduced forms of Pd/Al$_2$O$_3$ along with corresponding ratios for PdO and Pd-foil. Crystallographically well-defined PdO (ca. 2 m^2/g) was derived from base hydrolysis of aqueous Pd(NH$_3$)$_4$(NO$_3$)$_2$ followed by air calcination at 550°C. This material was further dehydrated by heating under vacuum to about 200°C prior to analysis. The ultra-high-purity Pd-foil (Materials Research Corp.) was cleaned by argon ion sputtering prior to analysis.

It is apparent from Table 4 that the magnitude of the Pd(3d)/Pd(MNN) XPS intensity ratio displayed a strong dependence on precalcination conditions. After brief calcination at 250°C, the ratio was reduced by about a factor of 2 compared to PdO,

FIG. 9. Pd(3d)/Pd(MNN) XPS intensity ratios normalized according to Eq. (13) are correlated with particle size for oxidic and reduced forms of 3.3% Pd/Al₂O₃. As summarized in Table 5, the predicted particle size increases with increasing calcination severity.
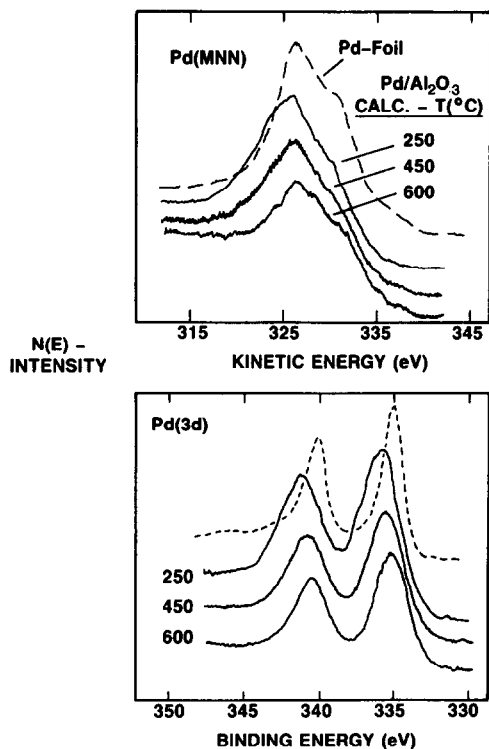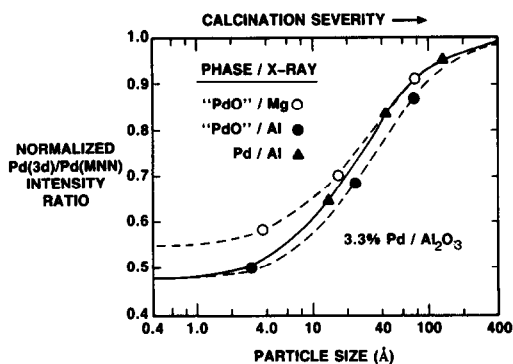

FIG. 8. Palladium (3d) XPS spectra and X-ray-excited Pd(MNN) Auger spectra are displayed for a 3.3% Pd/Al₂O₃ catalyst after air calcination at 250–600°C and *in situ* H₂ reduction at 500°C. The dashed curves correspond to a clean, polycrystalline Pd-foil surface. Catalyst binding energies are referred to Al(2s) at 119.0 eV.

whereas after overnight calcination at 600°C, the Pd(3d)/Pd(MNN) intensity ratio for Pd/Al₂O₃ approached that for PdO. Calcination at 450°C produced intermediate be-

havior. These changes appear to arise from sintering of the dispersed phase during high-temperature air treatment. As expected, sintering was accompanied by a sharp decrease in the magnitude of the Pd(3d)/Al(2s) XPS intensity ratio (I). Subsequent reduction studies were accompanied by a moderate (ca. 30%) decrease in both the Pd(3d)/Pd(MNN) and the Pd(3d)/Al(2s) XPS intensity ratios.

The size of the palladium-containing dispersed phase particles was estimated as before by combining Eqs. (3), (7), and (9), i.e., the diamond model assuming cubic dispersed phase morphology. Figure 9 illustrates these particle sizes plotted in the form of Fig. 2. Specifically, the normalized intensity ratio (NIR) is represented by

$$
\begin{aligned}
\mathrm{NIR} &= \frac{\beta(d, \lambda_2)}{\beta(d, \lambda_1)} \\
&= \frac{(I_{3d}/I_{\mathrm{MNN}})^{\mathrm{cat}}}{(I_{3d}/I_{\mathrm{MNN}})^{\mathrm{bulk}}} \frac{[1 + 2/(\sqrt{2}b/\lambda_{\mathrm{MNN}}^{\mathrm{Al_2O_3}}(1 - \exp(-\sqrt{2}b/\lambda_{\mathrm{MNN}}^{\mathrm{Al_2O_3}})) - 1)]}{[1 + 2/(\sqrt{2}b/\lambda_{3d}^{\mathrm{Al_2O_3}}(1 - \exp(-\sqrt{2}b/\lambda_{3d}^{\mathrm{Al_2O_3}})) - 1)]} \\
&= \frac{(1 - \lambda_{3d}^{\mathrm{Pd}}(1 - \exp(-\sqrt{2}d/\lambda_{3d}^{\mathrm{Pd}}))/\sqrt{2}d)}{(1 - \lambda_{\mathrm{MNN}}^{\mathrm{Pd}}(1 - \exp(-\sqrt{2}d/\lambda_{\mathrm{MNN}}^{\mathrm{Pd}}))/\sqrt{2}d)},
\end{aligned} \tag{13}
$$

where $b \simeq 227$ Å and the attenuation lengths and intensity ratios are those included in Table 4. It is evident that the pre-

treatment conditions investigated span the range of particle sizes which may be conveniently studied using the XPS intensity

TABLE 4

XPS Intensity Ratios and Attenuation Lengths for 3.3% Pd/Al$_2$O$_3$ Catalysts
with Variable Pretreatment

Precalcination conditions	XPS intensity ratios (±ca. 10%)			
	Pd(3d)/Pd(MNN)		Pd(3d)/Al(2s)	
	MgKα	AlKα	MgKα	AlKα
A. Unreduced catalysts				
250°C, 0.5 hr	0.67	0.54	0.89	0.70
450°C, 2 hr	0.81	0.74	0.59	0.49
600°C, 20 hr	1.06	0.95	0.34	0.32
PdO reference	1.10	1.01	—	—
B. Reduced catalysts[a]				
250°C, 0.5 hr	—	0.46	—	0.46
450°C, 2 hr	—	0.60	—	0.33
600°C, 20 hr	—	0.68	—	0.21
Pd reference	—	0.666	—	—
C. Material dependence of attenuation length (Å)				
Phase	λ_{MNN}(325 eV)	λ_{3d}(Al-1150 eV)		λ_{3d}(Mg-918 eV)
Pd	7.8	16.7		14.6
PdO	10.7	22.6		19.7
Al$_2$O$_3$	10.1	21.9		19.0

[a] After *in situ* H$_2$ treatment at 500°C, 1 atm, 2 hr.

ratio for two dispersed phase core levels. The particle size (or dispersed phase thickness) for oxidized palladium in calcined catalysts appeared to increase from about 4 Å at 250°C to roughly 75 Å at 600°C. The particle sizes estimated using MgKα and AlKα radiation agreed very closely. After H$_2$ treatment at 500°C, the palladium particle sizes appeared to increase to about 15–130 Å. This increase may reflect sintering of the dispersed phase during reduction, or it could also arise from hydrogen-induced restructuring of the particle morphology.

To test for self-consistency, the average size of the dispersed phase particles was also investigated using electron microscopy and static oxygen chemisorption. Table 5 summarizes particle sizes estimated using the various methods. Compared to the conventional methods it is apparent that analysis of the dispersed phase XPS intensity ratio generally provided reasonable estimates

for the particle size. Minor discrepancies with the most severely calcined catalyst can probably be explained by the fact that the XPS intensity ratio becomes relatively insensitive to particle size changes for $d \geq$ 2–3λ. In this circumstance, the accuracy of

TABLE 5

Dispersed Phase Particle Sizes for 3.3% Pd/Al$_2$O$_3$
Estimated by XPS, TEM, and O$_2$ Uptake

Precalcination conditions	Dispersed phase particle size (Å)				
	Unreduced catalysts		Reduced catalysts[a]		
	XPS	TEM	XPS	TEM	O$_2$ Uptake[b]
250°C, 0.5 hr	4	—	14	21	≤10 (O/Pd = 1.2)
450°C, 2 hr	21	30	43	44	49 (O/Pd = 0.28)
600°C, 20 hr	76	55	130	74	92 (O/Pd = 0.15)

[a] After 2 hr H$_2$ treatment at 500°C.
[b] Assuming cubic morphology and one oxygen atom per surface Pd atom.

TABLE 6

Dependence of Reduced Pd/Al_2O_3 Particle Size
Predictions on Magnitude of λ

Pd $\lambda_{3d}(\text{Å})^a$	Predicted particle size (Å) after precalcination at		
	250°C	450°C	600°C
8.4 (−50%)	8	27	180
12.8 (−30%)	11	36	140
16.8 (Std)	14	43	130
21.7 (+30%)	16	49	120
25.1 (+50%)	17	53	120

^{a} In each calculation, λ_{MNN}^{Pd}, $\lambda_{3d}^{Al_2O_3}$, and $\lambda_{MNN}^{Al_2O_3}$ were varied from standard by the same percentages.

the particle size prediction becomes strongly dependent upon the accuracy of the intensity ratio measurement which has an uncertainty of about ±10%. In a separate report (6), we show that, when roughness is considered in the analysis, very similar particle size predictions are obtained using the (Pd/Al) XPS intensity ratios included in Table 4.

Finally, it is of interest to explore how changes in the magnitude of the electron attenuation lengths influence the particle size predictions. Table 6 compares particle size estimates based on the diamond model using the "standard" attenuation lengths described earlier (Table 4, Ref. (14)) and hypothetical attenuation lengths which are assumed to be 30–50% smaller or larger than the standard values. It can be seen that the absolute magnitude of the attenuation lengths can have a significant influence on the particle size prediction. Specifically, with small particles, d is approximately proportional to λ_{Pd}. However, with larger particles, the size predictions are more strongly influenced by changes in intensity from microporous regions below the surface, e.g., changes in the factor represented by Eq. (9). In this case, d is predicted to increase as λ_{Pd} decreases.

CONCLUSIONS

A straightforward methodology for obtaining particle size information from photoemission results has been developed and exemplified by considering the intensity ratio for two dispersed phase core levels with different kinetic energy. Compared to earlier XPS methods, our approach displays a reduced sensitivity to catalyst physical properties, although the predicted particle size can be strongly influenced by the presence of contaminant overlayers. Many opportunities exist for applying this analysis in studies of both model and practical heterogeneous catalysts.

APPENDIX A: DERIVATION OF EQ. (6)

Figure A1 shows a cubic particle with edge length d supported on a surface with an arbitrary electron take-off angle $45° \leq \phi \leq 90°$. We calculate the XPS intensity for the cubic particle as a sum of intensities for the three indicated regions, R1–R3, that are subdivided along the x axis. For each region, the primary intensity is obtained by integrating Eq. (2) with an appropriate choice of the volume element, dV, such that material within this element is equidistant from the surface. For R1, $Z_1 = -d \sin \phi - x \cot \phi$, and
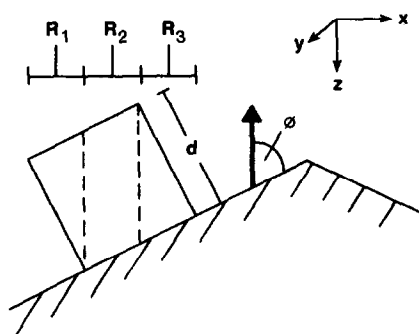

FIG. A1. Cubic particle on a triangular rough support surface with electron take-off angle ϕ.

$$I_1(d, \phi) = \rho\sigma T \int_o^d dy \int_o^{d\cos\phi} dx \int_{z_1}^{-d\sin\phi + x\tan\phi} \exp(-(z - z_1)/\lambda)dz$$

$$= \rho\sigma T\lambda d[d \cos \phi + (\lambda/(\tan \phi + \cot \phi))[\exp(-(\sin \phi + \cos \phi \cot \phi)d/\lambda) - 1]].$$
(A1)

For R2, z_1 remains unchanged and

$$I_2(d, \phi) = \rho\sigma T \int_o^d dy \int_{d\cos\phi}^{d\sin\phi} dx \int_{z_1}^{-(x - d\cos\phi)\cot\phi} \exp(-(z - z_1)/\lambda)dz$$

$$= \rho\sigma T\lambda d(d \sin \phi - d \cos \phi)(1 - \exp(-(\sin \phi + \cos \phi \cot \phi)d/\lambda)). \quad (A2)$$

Finally, for R3, $z_1 = -d \sin \phi - d \cos \phi + (x - d \sin \phi) \tan \phi$, and

$$I_3(d, \phi) = \rho\sigma T \int_o^d dy \int_{d\sin\phi}^{d\sin\phi + d\cos\phi} dx \int_{z_1}^{-(x - d\cos\phi)\cot\phi} \exp(-(z - z_1)/\lambda)dz$$

$$= \rho\sigma T\lambda d[d \cos \phi - (\lambda/(\tan \phi \cot \phi))[1 - \exp(-(\sin \phi + \cos \phi \cot \phi)d/\lambda)]].$$
(A3)

Combination of Eqs. (A1)–(A3) yields

$$I(d, \phi) = I_1(d, \phi) + I_2(d, \phi) + I_3(d, \phi)$$

$$= \rho\sigma T\lambda d^2 2 \cos \phi[1 - \tfrac{1}{2}(1 - \tan \phi + 2\lambda/(\sin \phi - \cot \phi \cos \phi)d)$$

$$(1 - \exp(-(\sin \phi + \cot \phi \cos \phi)d/\lambda))] \quad (A4)$$

which is equivalent to Eq. (6).

APPENDIX B: LAYER-BY-LAYER ANALYSIS OF INTENSITIES

For the slab model shown in Fig. 5, the total intensities for the support and dispersed phases can be represented as a sum of intensities for the individual layers. In the following we adopt the shorthand notation $\eta_m = F(L, s, d)\beta(d, \lambda_m)$. For the first dispersed phase layer,

$$I_{m1}(d) = \rho_m\sigma_m T_m\lambda_m A_o\eta_m, \quad (A5)$$

while for the second layer,

$$I_{m2}(d) \approx 2\rho_m\sigma_m T_m\lambda_m A_o\eta_m \exp(-b/\lambda_s),$$
(A6)

and, for the nth layer,

$$I_{mn}(d)$$

$$\approx 2\rho_m\sigma_m T_m\lambda_m A_o\eta_m \exp(-(n - 1)b/\lambda_s).$$
(A7)

Hence,

$$I_m(d) = \sum_{i=1}^{\infty} I_{mi}(d)$$

$$= \rho_m\sigma_m T_m\lambda_m\eta_m A_o \left[1 + 2 \sum_{i=1}^{\infty} \exp(-ib/\lambda_s)\right]$$

$$= \rho_m\sigma_m T_m\lambda_m\eta_m A_o[1 + 2/(\exp(b/\lambda_s) - 1)]. \quad (A8)$$

Similarly, for the diamond model using Eq. (A4) with $\phi = 45°$,

$$I_m(d) = \rho_m\sigma_m T_m\lambda_m\eta_m A_o \left[1 + 2 \sum_{i=1}^{\infty} [\lambda_s(1 - \exp(-\sqrt{2}b/\lambda_s))/\sqrt{2}b]^i\right]$$

$$= \rho_m\sigma_m T_m\lambda_m\eta_m A_o[1 + (2/\sqrt{2}b/\lambda_s(1 - \exp(-\sqrt{2}b/\lambda_s)) - 1)]. \quad (A9)$$

REFERENCES

1. Fung, S. C., *J. Catal.* **58**, 454 (1979).
2. Angevine, P. J., Vartuli, J. C., and Delgass, W. N., "Proceedings, 6th International Congress on Catalysis, London, 1976" (G. C. Bond, P. B. Wells, and F. C. Tompkins, Eds.). The Chemical Society, London, 1976.
3. Fadley, S. C., Baird, R. J., Siekhaus, W., Novakov, T., and Bergstrom, S. A. L., *J. Electron Spectrosc. Relat. Phenom.* **4**, 93 (1974).
4. Kerkhof, F. P. J. M., and Moulijn, J. A., *J. Phys. Chem.* **83**, 1012 (1979).
5. Seah, M. P., and Dench, W. A., *Surf. Interface Anal.* **1**, 2 (1979).
6. Davis, S. M., *J. Catal.*, in press.
7. Lindau, I., and Spicer, W. E., *J. Electron Spectrosc.* **3**, 409 (1974).
8. Wagner, C. D., Davis, L. E., and Riggs, W. M., *Surf. Interface Anal.* **2**, 53 (1980).
9. Powell, C. J., *Surf. Interface Anal.* **7**, 256 (1985); Powell, C. J., *Surf. Sci.* **44**, 29 (1974).
10. Tanuma, S., Powell, C. J., and Penn, D. R., *Surf. Sci.* **192**, L849 (1987).
11. Shirley, D. A., *Phys. Rev. B.* **5**, 4709 (1972).
12. Tougaard, S., *Surf. Sci.* **162**, 875 (1985); Tougaard, S., and Jorgensen, B., *Surf. Sci.* **143**, 482 (1984); Tougaard, S., and Sigmund, P., *Phys. Rev. B.* **25**, 2452 (1982).
13. Davis, S. M., and Somorjai, G. A., *Bull. Soc. Chim. Fr.*, 271 (1985).
14. All the electron attenuation lengths used in this report represent an averge between λ-values predicted using the formulas proposed in Refs. (5) and (10). With the exception of PdO, these λ-values normally differed by less than 15%.